World Scientific
www.worldscientific.com

JAPAN SOCIETY OF CIVIL ENGINEERS
COASTAL ENGINEERING COMMITTEE

Coastal Engineering Journal, Vol. 52, No. 3 (2010) 235–259

DOI: 10.1142/S0578563410002166

MULTIPHASE MODELING OF WAVE PROPAGATION OVER SUBMERGED OBSTACLES USING WENO AND LEVEL SET METHODS

TAMER H. M. A. KASEM* and JUN SASAKI†

Department of Civil Engineering, Graduate School of Engineering,
Yokohama National University, Tokiwadai, Hodogaya-ku,
Yokohama, 240-8501, Japan
** d07sc192@ynu.ac.jp*
† jsasaki@ynu.ac.jp

Received 11 September 2009
Revised 13 August 2010

A new numerical multiphase model is presented to study wave propagation over arbitrary shaped submerged obstacles. The high order space accurate weighted essentially non-oscillatory (WENO) method is adopted along with relatively coarse Cartesian uniform grids. Viscosity effects are included and the free surface is tracked using the level set method. The model is validated via application to solitary and progressive wave motion over rectangular, trapezoidal and semicircular obstacles. The complex flow field features induced near a large sized obstacle, including separation vortices and large free surface deformations, are accurately reproduced. Compared to other relatively complicated models, the present model is efficient and produces enhanced results.

Keywords: Numerical wave model; Navier Stokes; WENO; level set; submerged obstacle; finite difference.

1. Introduction

Studying the problem of wave propagation over submerged obstacles (abbreviated as WPSO) is important for coastal engineers [Huang and Dong, 2001; Zhuang and Lee, 1996; Tang and Chang, 1998]. Chang *et al.* [2001] cited several works dealing with WPSO and emphasized its importance in modeling submerged breakwaters. In general, two methods exist to study WPSO; the first choice consists of laboratory studies and field programs; and the second choice is using numerical modeling. The latter choice is more economic in terms of the required working space and facilities, operating costs and technical staff [Kamphuis, 2000].

For WPSO, vortex shedding usually occurs near the obstacle [Chang *et al.*, 2001; Huang and Dong, 2001; Tang and Chang, 1998]. Accurate modeling of this rotational flow field is necessary due to its impact on sediment motion near a submerged breakwater [Zhuang and Lee, 1996; Chang *et al.*, 2001]. Also, strong free surface deformations may occur for relatively large sized obstacles [Cooker *et al.*, 1990]. Consequently, a numerical model used to simulate WPSO problem should provide accurate results for both flow vortices and highly deformed free surfaces.

Numerical models used to simulate WPSO can be classified into two types: single phase models and multiphase models. The studies of Zhuang and Lee [1996] and Tang and Chang [1998] belong to the former. Both studies focused on modeling of the separated flow field behind an obstacle. However, the free surface was tracked indirectly; using the potential flow solution [Zhuang and Lee, 1996], or adopting a moving curvilinear grid [Tang and Chang, 1998]. Consequently, their results were limited to obstacles of height to a depth ratio of 0.5 and relatively small free surface deformations.

Three widely used multiphase numerical models are "COBRAS" [Lin and Liu, 1998], "VOFbreak^2" [Troch and De-Rouk, 1998, 1999] and "CADMAS-SURF" [Interim Development Committee of a Numerical Wave Flume for Maritime Structure Design, 2001; Isobe *et al.*, 1999]. The free surface is tracked in these three models using "Volume-of-Fluid" method (VOF) adopting a fixed grid. However upon using these models to simulate WPSO, difficulties may occur.

The discretization scheme of the advection terms of Navier Stokes equations plays a key role in modeling WPSO. In general, two classes of discretization methods exist [Ekaterinaris, 2005]: high order methods (abbreviated as HOM) and low order methods (abbreviated as LOM). In practical codes, LOM are preferred [Ekaterinaris, 2005]. A major disadvantage of LOM is inducing excessive numerical diffusion leading to premature deformation and dissipation of flow vortices [Ekaterinaris, 2005]. As a consequence, LOM require extremely fine grids to accurately describe vortical flow fields, leading to large computational effort. This may be circumvented by using non-uniform grids as done in COBRAS, VOFbreak^2, and CADMAS-SURF. In this option, finer grids are located at the regions of high gradients. However other complications occur upon using a non-uniform grid: first, very small or large values for the horizontal vertical grid division ratio lead to numerical problems [Ferziger and Peric, 2002]; second, providing a suitable non-uniform grid for modeling WPSO where vortices and highly deformed free surfaces occur simultaneously may be rather difficult; finally, more effort is needed for grid generation or transformation depending on the obstacle shape. With an increasing concern about coastal environment and the high value of structures, the geometries of recent coastal structures are becoming more complex [Lee and Mizutani, 2009]. As a result, an approach that can handle arbitrary geometry with high efficiency while adopting the rather simple uniform grid is extremely valuable. Coarser grids can be used with HOM. Considering second order LOM the error is reduced by a factor of 1/4 if the grid size is doubled. While for fifth

order HOM the reduction factor is 1/32 [Ekaterinaris, 2005]. Consequently reliable computational results can be obtained with a uniform grid and the non-uniform grid complications can be avoided.

Two widespread methods to capture the free surface adopting a fixed grid are VOF [Hirt and Nichols, 1981] and Level Set method [Osher and Sethian, 1988]. Generally both VOF and level set methods capture the free surface by solving the same interface equation [Kothe *et al.*, 1998]. A crucial step for solving this equation in VOF is free surface "Reconstruction" [Scardovelli and Zaleski, 1999; Pilliod and Puckett, 2004]. This step is not simple [Sethian and Smereka, 2003]. The reconstruction scheme of the version of VOF proposed by Hirt and Nichols [1981] (used in COBRAS, VOFbreak^2, and CADMAS-SURF) may generate a large amount of artificial drops and bubbles [Scardovelli and Zaleski, 1999]. Reconstruction is avoided in the level set method, and the interface equation is solved using an accurate solver. This is the reason why level set is a simple alternative compared to VOF.

The weighted essentially non-oscillatory (WENO) method [Jiang and Shu, 1996] is one of the relatively modern discretizaion methods. According to the review of Ekaterinaris [2005], WENO belongs to HOM. WENO is an enhanced version of ENO method, which was applied extensively to multiphase flow [Sussman *et al.*, 1994; Chang *et al.*, 1996; Sussman *et al.*, 1998]. An important advantage of WENO is its versatility. This method was applied extensively to compressible flow [Ekaterinaris, 2005] and recently to single phase incompressible flow [Choi *et al.*, 2007; Zhang and Jackson, 2009].

The purpose of the present work is to develop a new multiphase model based on WENO and level set methods and designed for simulating WPSO on a uniform Cartesian grid. The advantages of WENO are exploited through application to the convection terms of Navier Stokes equations. Also WENO is incorporated in the level set algorithm to solve the hyperbolic interface equation. The model abilities of modeling WPSO features, including separation vortices and free surface deformation, are tested through simulating three types of obstacles: rectangular, trapezoidal and semicircular. The model efficiency is illustrated by comparing the results of existing models and experimental measurements. The model capabilities of computing the relatively complex case of a large sized semicircular obstacle (radius to depth ratio 0.7 and 0.8) are emphasized.

2. Numerical Formulation

2.1. *Governing equations*

Neglecting surface tension, for a two-phase gas-liquid flow, the incompressible Navier Stokes equations can be written in dimensionless form as [Sussman *et al.*, 1994]:

$$\frac{\partial u_j}{\partial x_j} = 0 \tag{1a}$$

$$\frac{\partial u_i}{\partial t} = -\frac{\partial (u_i u_j)}{\partial x_j} + \frac{1}{\rho R_e}\left[\frac{\partial\{\mu(\frac{\partial u_i}{\partial x_j} + \frac{\partial u_j}{\partial x_i})\}}{\partial x_j}\right] - \frac{1}{\rho}\frac{\partial P}{\partial x_i} - \frac{L_\infty}{U_\infty^2} g_i \qquad (1b)$$

Equations (1a) and (1b) are the continuity and momentum equations, respectively, where u_i is the dimensionless velocity in the i direction. g_i is the gravity force defined using Kronecker delta as $g_i = -9.8\delta_{i2}$. In Eq. (1) the index $i = 1, 2$ stands for the horizontal and vertical x, y directions, respectively; L_∞ and U_∞ are the reference length and velocity scales, respectively; R_e is the dimensionless Reynolds number defined as $R_e = \rho_\infty U_\infty L_\infty / \mu_\infty$; P, ρ and μ are the dimensionless pressure, density and viscosity that are normalized using $\rho_\infty U_\infty^2$, ρ_∞ and μ_∞, respectively.

Choi *et al.* [2007] solved Eq. (1) using WENO method and adopting the concept of artificial compressibility which is a tunable parameter. In the present model, similar to the work of Zhang and Jackson [2009] this tunable parameter is not used. In the present work, Eq. (1) is solved using a methodology that is similar to the MAC method. A staggered grid is adopted. Viscous and convective terms on the right-hand side of Eq. (1b) are discretized using variables at the current time step n. The divergence free constraint [Eq. (1a)] is fulfilled, and the pressure is computed by solving a Poisson equation for pressure (PPE). Finally, the velocity components at step $n+1$ are evaluated. For more details on the MAC method, the reader is referred to Fletcher [1991]. The primary time-consuming step in this procedure is to solve the system of linear equations resulting from PPE. In the present work, the Bi-CGSTAB method is used with point Jacobi preconditioning [Barrett *et al.*, 1993]. In the original MAC method, both viscous diffusion and convection terms are discretized using centered second order difference formulae. For convection dominated problems, such discretization leads to severe non-physical oscillations [Fletcher, 1991].

In the present model, unlike the original MAC method, convection terms are discretized using WENO fifth order space accurate method. More details about the WENO method are given in Subsec. 2.2. Multiphase flow is studied in the current work using the level set method. Details of the level set algorithm are presented in Subsec. 2.3.

2.2. *WENO method*

In this subsection, essentials of the WENO fifth order method are presented based on the explanation provided by Shu [1998]. First, discretization in the horizontal direction is described. The extension to multi-dimensions will be shown later. The convection term at grid point i is discretized as:

$$\left.\frac{\partial (uf)}{\partial x}\right|_i = \frac{\widehat{uf}_{i+1/2} - \widehat{uf}_{i-1/2}}{\Delta x} + O(\Delta x^5) \qquad (2)$$

Here, Δx is the horizontal grid size, f stands for any convected quantity, including u and v in the horizontal and vertical momentum equations, respectively. In Eq. (2), $\widehat{uf}_{i-1/2}$ presents the numerical flux to the left of point i. The aim of using WENO is to capture high gradients in a stable manner while providing high resolution for regions of smooth gradients. To accomplish this goal the value of the fluxes ($\widehat{uf}_{i-1/2}$) should be calculated carefully. Two possible approximations that exist for $\widehat{uf}_{i-1/2}$ are; $\widehat{uf}^{+}_{i-1/2}$ (down-wind), and $\widehat{uf}^{-}_{i-1/2}$ (up-wind). The former is obtained using the values at grid points $i-2$, $i-1$, i, $i+1$ and $i+2$ (i.e. stencil $[i-2, i+2]$), while $\widehat{uf}^{-}_{i-1/2}$ is obtained if the stencil $[i-3, i+1]$ is used. First, equations for both approximations are presented, and then the criterion for the choice among them will be explained.

For the down-wind and up-wind approximations, the flux $\widehat{uf}_{i-1/2}$ is given by

$$\widehat{uf}_{i-1/2} = \sum_{s=0}^{s=2} \tilde{\omega}_s \overline{uf}_s \tag{3}$$

The terms that appear in Eq. (3) are calculated using Eq. (4) to Eq. (8):

$$\left.\begin{aligned}
\beta_0 &= \frac{13}{12}(u_i f_i - 2u_{i+1}f_{i+1} + u_{i+2}f_{i+2})^2 + \frac{1}{4}(3u_i f_i - 4u_{i+1}f_{i+1} + u_{i+2}f_{i+2})^2 \\
\beta_1 &= \frac{13}{12}(u_{i-1}f_{i-1} - 2u_i f_i + u_{i+1}f_{i+1})^2 + \frac{1}{4}(u_{i-1}f_{i-1} - u_{i+1}f_{i+1})^2 \\
\beta_2 &= \frac{13}{12}(u_{i-2}f_{i-1} - 2u_{i-1}f_{i-1} + u_i f_i)^2 + \frac{1}{4}(u_{i-2}f_{i-2} - 4u_{i-1}f_{i-1} + 3u_i f_i)^2
\end{aligned}\right\} \tag{4a}$$

$$\left.\begin{aligned}
\beta_0 &= \frac{13}{12}(u_{i-1}f_{i-1} - 2u_i f_i + u_{i+1}f_{i+1})^2 + \frac{1}{4}(3u_{i-1}f_{i-1} - 4u_i f_i + u_{i+1}f_{i+1})^2 \\
\beta_1 &= \frac{13}{12}(u_{i-2}f_{i-2} - 2u_{i-1}f_{i-1} + u_i f_i)^2 + \frac{1}{4}(u_{i-2}f_{i-2} - u_i f_i)^2 \\
\beta_2 &= \frac{13}{12}(u_{i-3}f_{i-3} - 2u_{i-2}f_{i-2} + u_{i-1}f_{i-1})^2 \\
&\quad + \frac{1}{4}(u_{i-3}f_{i-3} - 4u_{i-2}f_{i-2} + 3u_{i-1}f_{i-1})^2
\end{aligned}\right\} \tag{4b}$$

$$\tilde{d}_0 = 0.1\,, \quad \tilde{d}_1 = 0.6\,, \quad \tilde{d}_2 = 0.3 \tag{5a}$$

$$\tilde{d}_0 = 0.3\,, \quad \tilde{d}_1 = 0.6\,, \quad \tilde{d}_2 = 0.1 \tag{5b}$$

$$\tilde{\alpha}_k = \frac{\tilde{d}_k}{(\varepsilon + \beta_k)^2} (k = 0, 1, 2) \tag{6}$$

$$\tilde{\omega}_k = \frac{\tilde{\alpha}_k}{\sum_{s=0}^{s=2} \tilde{\alpha}_s} (k = 0, 1, 2) \tag{7}$$

$$\left.\begin{aligned}
\overline{uf}_0 &= \frac{11}{6}u_i f_i - \frac{7}{6}u_{i+1}f_{i+1} + \frac{1}{3}u_{i+2}f_{i+2} \\
\overline{uf}_1 &= \frac{1}{3}u_{i-1}f_{i-1} + \frac{5}{6}u_i f_i - \frac{1}{6}u_{i+1}f_{i+1} \\
\overline{uf}_2 &= -\frac{1}{6}u_{i-2}f_{i-2} + \frac{5}{6}u_{i-1}f_{i-1} + \frac{1}{3}u_i f_i
\end{aligned}\right\} \tag{8a}$$

$$\left.\begin{aligned}
\overline{uf}_0 &= \frac{1}{3}u_{i-1}f_{i-1} + \frac{5}{6}u_i f_i - \frac{1}{6}u_{i+1}f_{i+1} \\
\overline{uf}_1 &= \frac{1}{6}u_{i-2}f_{i-2} + \frac{5}{6}u_{i-1}f_{i-1} + \frac{1}{3}u_i f_i \\
\overline{uf}_2 &= \frac{1}{3}u_{i-3}f_{i-3} - \frac{7}{6}u_{i-2}f_{i-2} + \frac{11}{6}u_{i-1}f_{i-1}
\end{aligned}\right\} \tag{8b}$$

Here, ε in Eq. (6) is an arbitrarily small parameter used to avoid division by zero. The equations appended with letter a [Eqs. (4a), (5a) and (8a)] and those appended with letter b [Eqs. (4b), (5b) and (8b)] correspond to down-wind and up-wind discretizations, respectively.

Lax-Friedrichs flux splitting is adopted to determine the choice between up-wind and down-wind as follows:

$$\widehat{uf}_{i-1/2} = \begin{cases} \widehat{uf}^{+}_{i-1/2} & u_i \& u_{i-1} < 0 \\ \widehat{uf}^{-}_{i-1/2} & u_i \& u_{i-1} > 0 \\ \widehat{uf}^{*}_{i-1/2} & \text{else} \end{cases} \tag{9}$$

where $\widehat{uf}^{*}_{i-1/2}$ is the sum of both the down-wind flux of $(uf - \alpha f)/2$ and the up-wind flux of $(uf + \alpha f)/2$, and $\alpha = \max|u_i|$.

For the two-dimensional case, Eq. (2) can be rewritten as:

$$\left.\frac{\partial(uf)}{\partial x}\right|_{i,j} + \left.\frac{\partial(vf)}{\partial y}\right|_{i,j} \cong \frac{\widehat{uf}_{i+1/2,j} - \widehat{uf}_{i-1/2,j}}{\Delta x} + \frac{\widehat{vf}_{i,j+1/2} - \widehat{vf}_{i,j-1/2}}{\Delta y} \tag{10}$$

Here, Δy is the vertical grid size. The vertical and horizontal fluxes computation steps are totally independent. The rectangular domain can be swept horizontally where the horizontal term $\partial(uf)/\partial x|_{i,j}$ is computed. This step can be followed by another vertical sweep where the vertical term $\partial(vf)/\partial y|_{i,j}$ is computed and added to the already calculated terms.

2.3. *Level set method*

In the current work, multiphase flow is modeled using the level set method, where liquid and gas regions are identified using the color function ϕ. Two forms of ϕ exist in the literature [Kasem and Sasaki, 2009]. One discontinuous form is generated by

assigning ϕ a value of one and zero in liquid and gas regions, respectively. Another form results upon equating ϕ to the distance from the gas-liquid interface. For both forms, the time variation of ϕ is governed by:

$$\frac{\partial \phi}{\partial t} + \nabla \cdot (\boldsymbol{V}\phi) = 0 \tag{11}$$

where $\boldsymbol{V}$ is the fluid velocity vector. Various methods exist to solve Eq. (11). Kasem and Sasaki [2009] studied choices related to those two forms of ϕ. They also tested two numerical solvers of Eq. (11): WENO method, and CIP-CSL3 method proposed by Xiao and Yabe [2001]. Kasem and Sasaki [2009] demonstrated that the discontinuous form yields a broad irregular free surface interface compared to the distance formulation. Their results are consistent with the review of Kothe *et al.* [1998] who reported that the discontinuous form leads to unacceptable broadening of the interface. Kasem and Saski [2009] also emphasized the efficiency of WENO compared to CIP-CSL3. As a result, they concluded that using the distance formulation for ϕ and WENO method to solve Eq. (11) is the optimum choice among other alternatives. In the present work, this choice will be adopted.

The shape of ϕ near the interface is illustrated in Fig. 1 along with the relevant parameters. The interface thickness δ is defined as $\delta = (\phi_{\max} - \phi_{\min})/2 = 1.5\Delta$, where Δ is the numerical grid size [Sussman *et al.*, 1994]. For an incompressible fluid, the fluid properties of interest are the density ρ and the viscosity μ. These properties are calculated using Eq. (12):

$$\rho = \rho_L \phi_{\text{comp}} + \rho_G (1 - \phi_{\text{comp}}) \quad \mu = \mu_L \phi_{\text{comp}} + \mu_G (1 - \phi_{\text{comp}}) \tag{12}$$

where μ_L, ρ_L, μ_G and ρ_G are the dynamic viscosities and densities of liquid and gas, respectively. ϕ_{comp} is computed from ϕ using Eq. (13).

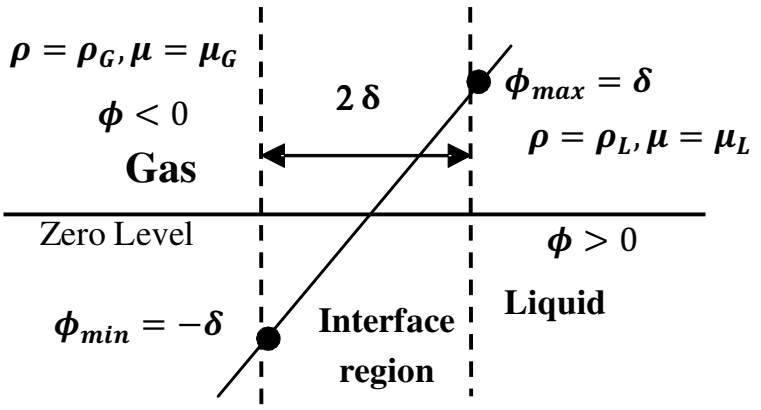

Fig. 1. Typical form of ϕ near the gas–liquid interface.

$$\phi_{\text{comp}} = \begin{cases} 0 & \text{if } \phi < -\delta \\ 1 & \text{if } \phi > \delta \\ 0.5\left\{1 + \sin\left(\dfrac{\pi\phi}{2\delta}\right)\right\} & \text{else} \end{cases} \tag{13}$$

An important step to be done after solving Eq. (11) using WENO is re-initialization [Sussman and Fatemi, 1999; Sussman *et al.*, 1998]. This step assures that the slope of ϕ is kept equal to unity. The re-initialization algorithm is detailed in Appendix A.

2.4. *Boundary conditions*

Boundary conditions are classified into three categories: bottom and top boundaries, irregular boundaries and sponge layer boundaries. At the bottom boundary, no-slip wall boundary condition is imposed [Wang *et al.*, 2009; Hieu and Tanimoto, 2006]. At the top boundary, no-normal gradient wall boundary condition is applied [Park *et al.*, 1999].

2.4.1. *Irregular boundaries*

In the present work, wave propagation over arbitrarily shaped submerged bodies is studied. Modeling such irregularly shaped boundary problems using a Cartesian uniform grid is done using the "Blocked-off Regions" method. The blocked-off regions method is rather straightforward as described by Patankar [1980]. The same discretization is done for all grid points. However, for grid points inside the stationary solid body, the velocity is assigned to zero. Patankar [1980] reported that surprisingly good answers can often be obtained using such a simple method.

2.4.2. *Sponge layer formulation*

Following the methodology of Troch and De-Rouk [1999], "absorbing boundary" conditions are implemented at the lateral boundaries. The purpose for using these conditions is to minimize the effects of waves reflected from the domain boundaries. An absorbing function is applied to the flow variables near the domain lateral boundaries. The absorbing function is given by:

$$a_1(x) = \sqrt{1 - \left(\frac{x - x_1}{x_s}\right)^2} \tag{14}$$

where x_1 is the location of the edge of the sponge layer, and x_s is the sponge layer width. It is clear that the function varies gradually from $a_1(x_1) = 1$, which provides no damping at the edge of the layer, to $a_1(x_1 + x_s) = 0$, which provides total damping at the far edge of the domain. In the present work, damping is applied to the vertical velocity.

3. Results and Discussion

3.1. *Solitary wave propagation over a submerged rectangular obstacle*

In this subsection, the verification of the proposed model by simulating the propagation of a solitary wave over a submerged rectangular obstacle is described. The problem domain and setup are sketched in Fig. 2. Measurements made by Zhuang and Lee [1996] are used to validate the current model results. In the present example, the reference length and velocity scales are defined as $L_\infty = d$ and $U_\infty = \sqrt{gd}$. In Table 1, the definition of the dimensionless parameters that govern the problem, along with the values corresponding to the experiment performed by Zhuang and Lee [1996] are shown. Zhuang and Lee [1996] provided LDV measurements of horizontal and vertical velocity components (u and v respectively) at the two fixed locations (pt1 and pt2) shown in Fig. 2. Sponge layers are used at the lateral boundaries to minimize reflection effects. The sponge layer width is set to $3d$ and $0.5d$ at the left and right boundaries, respectively. The dimensions of the computational domain are $X_{\max} = 45d$ and $Y_{\max} = 1.6d$. The number of uniform grid subdivisions is 855×96 cells in the horizontal and vertical directions, respectively. The maximum

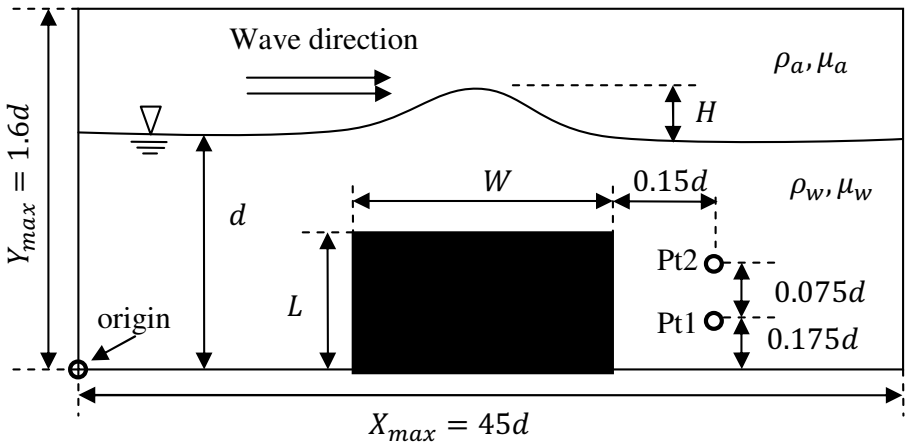

Fig. 2. Definition of the problem of solitary wave propagation over a rectangular obstacle.

Table 1. Problem parameter definitions and values for solitary wave propagation over a rectangular obstacle.

Parameter	Dimensionless wave height	Reynolds number	Air-water density ratio	Air-water viscosity ratio	Dimensionless obstacle width	Dimensionless obstacle height
Definition	H/d	$R_e = \frac{\sqrt{g}d^{1.5}\rho_w}{\mu_w}$	$\frac{\rho_a}{\rho_w}$	$\frac{\mu_a}{\mu_w}$	W/d	L/d
Value	0.3	3.41×10^5	1.2×10^{-3}	1.97×10^{-2}	1.67	0.5

simulation time is $t\sqrt{(g/d)} = 27.8$, with 42,000 time steps. The left face of the obstacle is located at $13.33d$ from the origin. The solitary wave peak is initiated at $X = 8d$.

Initial conditions for η (the free surface height measured from the bottom) and fluid velocities are given by [Lee *et al.*, 1982]:

$$\frac{\eta}{d} = 1 + \frac{H}{d}\left(\text{sech}\left[(\sqrt{(3H/4d)}\frac{X}{d}\right]\right)^2 \tag{15a}$$

$$\frac{u}{\sqrt{gd}} = \frac{\eta}{d} - 1 \tag{15b}$$

$$\frac{v}{\sqrt{gd}} = \frac{y}{d}\left(\frac{\eta}{d} - 1\right)\sqrt{(3H/d)}\left(\tanh\left[\sqrt{(3H/4d)}\frac{X}{d}\right]\right) \tag{15c}$$

Numerical results of the present model are shown in Fig. 3. Numerical results by Chang *et al.* [2001] and the measurements made by Zhuang and Lee [1996] are shown in the same figure. The numerical results of Chang *et al.* [2001] were obtained using COBRAS with a non-uniform grid of minimum spacing of $0.0109d$ near the obstacle. The horizontal and vertical spacing of our model is $0.053d$ and $0.0167d$, respectively. Compared to the finest grid adopted by Chang *et al.* [2001] the spacing of our model is approximately 5 and 1.6 times larger in the horizontal and vertical directions, respectively. Referring to Fig. 3, our results based on a relatively coarse and simple grid, are closer to the measurements than those of COBRAS. Such enhancement is clearly observed for the horizontal velocity results.

In Fig. 4, stream lines and the free surface location are plotted near the rectangular obstacle at six instants. The prevailing feature is the separation vortex that is located downstream from the obstacle. The vortex size increases with time, and the vortex motion survives even after the solitary wave travels away from the obstacle. These results are consistent with the experiment performed by Zhuang and Lee [1996]. Unlike our model, Zhuang and Lee [1996] considered the viscous effects in their numerical calculation to be present only in the wake to the right of the obstacle. In the rest of the domain, inviscid irrotational flow is assumed, and the boundary element method was adopted. These assumptions should result in a faster computation time. However, with this method regions where viscous effects are present should be known in advance. The numerical model of Zhuang and Lee [1996] did not predict the small vortex on the top left of the obstacle that is shown in Fig. 4. The presence of this vortex was verified by Chang *et al.* [2001] for a similar case. In the present method, viscous effects are included in the whole domain in a direct and simple manner, which leads to more reliable results.

Another remarkable feature of the current work is that the velocity fields are revealed for both the air layer (gas phase) and the water layer (liquid phase). It should be noted that verification of the air flow results is a challenging task. Unfortunately

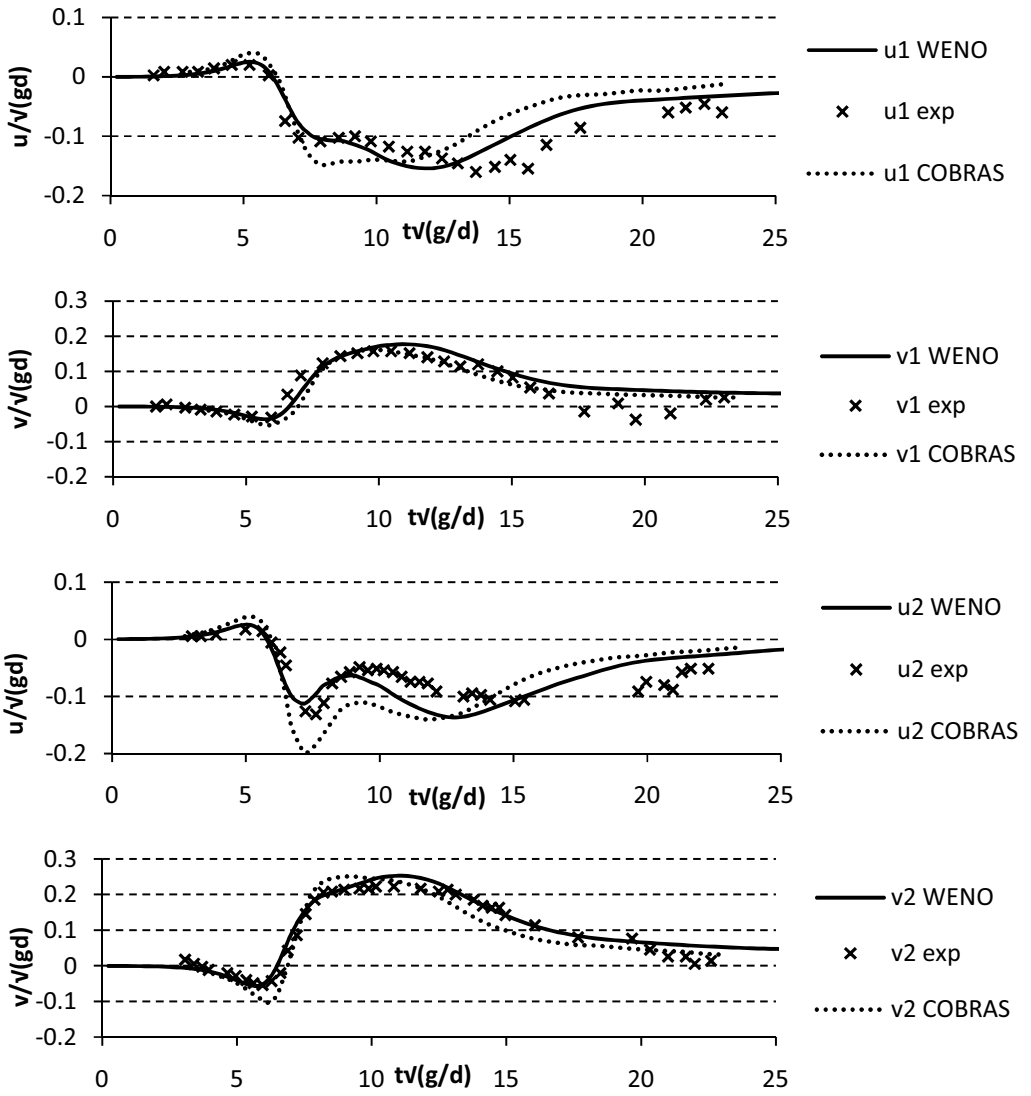

Fig. 3. Horizontal and vertical velocity versus time at points 1 and 2: u1 and v1 are the horizontal and vertical velocity components at point 1, while u2 and v2 are the velocity components at point 2.

in many studies, only the results of the liquid phase were presented, either for simulations [Lin and Liu, 1998; Wang *et al.*, 2009; Troch and De-Rouk, 1998, 1999], or for experiments [Chang *et al.*, 2001; Zhuang and Lee, 1996]. This is expected because the main focus of the mentioned works was to study the liquid phase.

In fact experimental results of the air velocity for the present problem (air flow over a solitary wave) were not found in the literature. A reliable method for validating air velocities is the comparison with the analytical results of the problem of internal solitary wave. In this problem, the motion of two horizontal layers of fluids

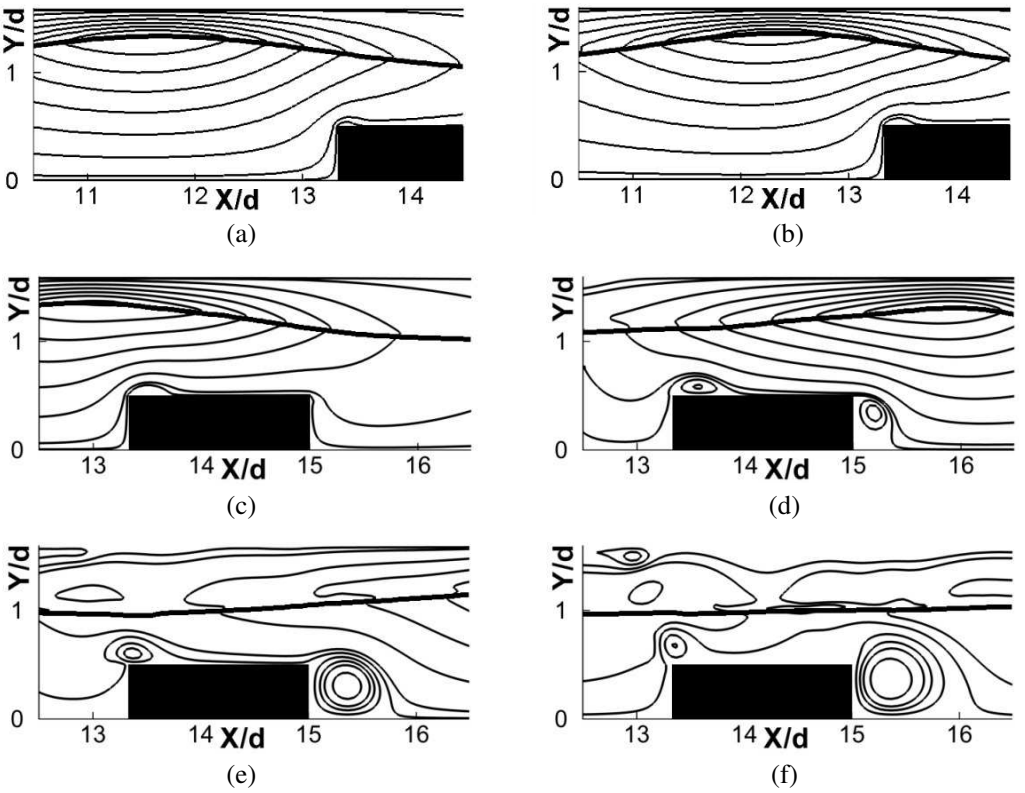

Fig. 4. Plot of stream lines and free surface location (thick line) near the rectangular obstacle at four instants: (a) $t\sqrt{(g/d)} = 3.24$; (b) $t\sqrt{(g/d)} = 3.94$; (c) $t\sqrt{(g/d)} = 4.63$; (d) $t\sqrt{(g/d)} = 6.95$; (e) $t\sqrt{(g/d)} = 9.267$; and (f) $t\sqrt{(g/d)} = 11.58$.

with two different densities is analyzed. If the two fluids are considered as water and air, strong similarity between this problem and the current one exists [Long, 1956; Hoyler, 1979]. Theoretically, a sharp velocity gradient exists at the interface between the two fluids [Keulegan, 1953; Lamb, 1906]. According to the analysis of Keulegan [1953], assuming potential flow over a constant depth, an analytical formula for the ratio between the velocities at the interface is given by:

$$\frac{u_w}{u_a} = -\frac{H_a}{H_w}\left[1 - \left(1 - \frac{\rho_a}{\rho_w}\right)\frac{1}{1 + H_a/H_w}\right] \tag{16}$$

where the subscripts w and a stand for water and air regions, respectively, H_w and H_a are the thickness of water and air layers, respectively. For the current numerical domain ($Y_{\max} = 1.6d$), the ratio between the thickness of air and water layers is $H_a/H_w = 0.6$, leading to $u_w/u_a = -0.225$. On the other hand, if the vertical domain size is increased to $Y_{\max} = 1.8d$, we get $H_a/H_w = 0.8$ and $u_w/u_a = -0.356$. Consequently, it is expected that a larger domain will yield lower air velocities.

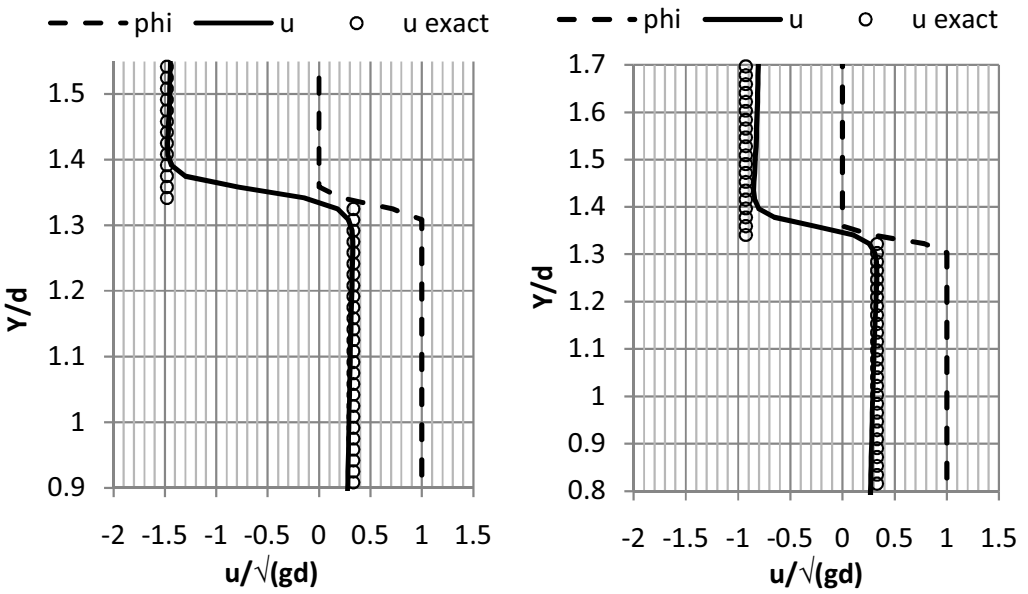

Fig. 5. Vertical profile of the horizontal velocity near the interface at wave peak at $X/d = 11.5$. Left are the results for a domain size $Y_{\max} = 1.6d$, right are the results for a domain size $Y_{\max} = 1.8d$.

To verify the consistency of the computational results with Eq. (16), the computed vertical profile of the horizontal velocity is shown in Fig. 5. The profile location and the time are selected at $X/d = 11.5$ and $t\sqrt{(g/d)} = 3.24$, respectively. The profile is plotted at a station far enough upstream from the obstacle, and at an instant early enough before the wave crest approaches the obstacle, so that Eq. (16) will be valid. The potential model velocity (u exact) is plotted based on Eqs. (15b) and (16). The current numerical model results (u) are also shown. The profile is plotted for two computational domains whose parameters are identical, except for the vertical domain size. The numerical model results yield high velocity gradient near the interface, $u_w/u_a \approx -0.225$ for $Y_{\max} = 1.6d$, and $u_w/u_a \approx -0.356$ for $Y_{\max} = 1.8d$. The value of ϕ_{comp} (phi) exhibits a rapid transition from one to zero at the interface as expected. These features agree well with the analytical results.

3.2. *Progressive periodic wave propagation over a submerged trapezoidal obstacle*

Next, our model is verified by simulating the propagation of progressive periodic waves over a trapezoid. The problem domain and setup are sketched in Fig. 6. Measurements made by Beji and Battjes [1994] are used for comparison.

Similar to Subsec. 3.1, the reference length and velocity scales are defined as $L_\infty = d$ and $U_\infty = \sqrt{gd}$. The dimensionless parameters governing the problem are given in Table 2. In addition to the dimensionless parameters mentioned in Subsec. 3.1, two extra parameters affect the progressive wave problem: $\bar{L} = L_w/d$,

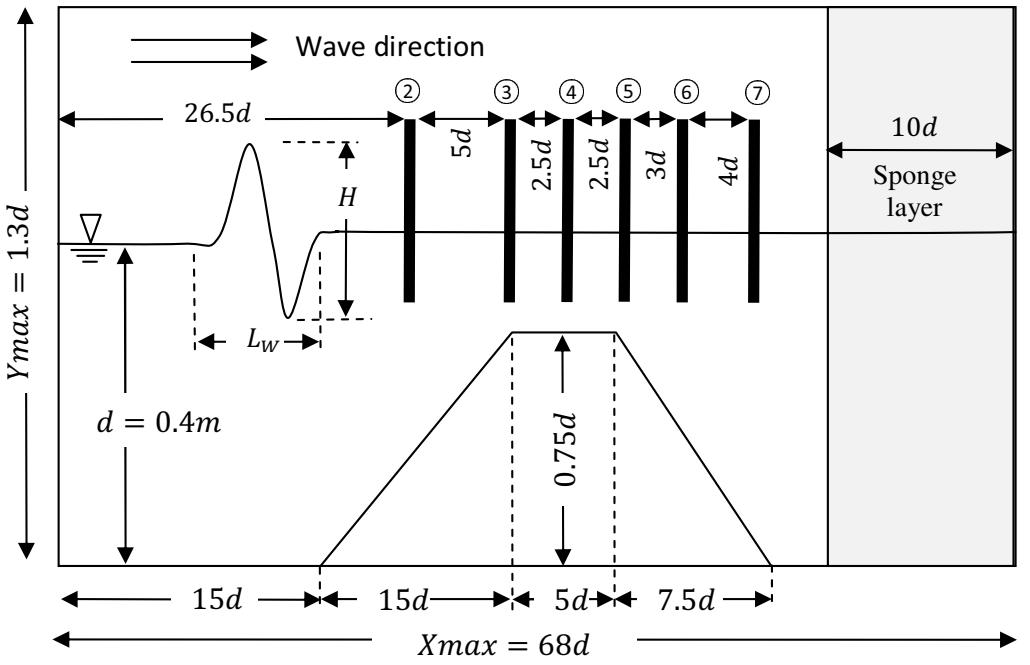

Fig. 6. Definition of the problem of progressive wave propagation over a trapezoidal bar.

Table 2. Parameter definitions and values for progressive wave propagation over a trapezoid.

Parameter	Dimensionless wave height	Dimensionless wave length	Dimensionless wave period	Reynolds number	Air-water density ratio	Air-water viscosity ratio
Definition	$\bar{H} = H/d$	$\bar{L} = L_w/d$	$\bar{T} = T\sqrt{g/d}$	$R_e = \frac{\sqrt{g}d^{1.5}\rho_w}{\mu_w}$	$\frac{\rho_a}{\rho_w}$	$\frac{\mu_a}{\mu_w}$
Value	0.05	9.232	9.8995	7.888×10^5	1.2×10^{-3}	1.97×10^{-2}

and $\bar{T} = T\sqrt{(g/d)}$, which are the dimensionless wave length and period, respectively. Both parameters are related by the dispersion relation [Dean and Dalrymple, 1984]:

$$\frac{2\pi}{\bar{T}^2} = \frac{\tanh(2\pi/\bar{L})}{\bar{L}} \tag{17}$$

The incoming waves are generated using Stokes second order wave theory [Dean and Dalrymple, 1984]:

$$\eta/d = 1 + \frac{\bar{H}}{2}\cos(k\bar{x} - \sigma\bar{t}) + \frac{\bar{H}^2\pi}{8\bar{L}}\frac{\cosh(k)}{[\sinh(k)]^3}[2 + \cosh(2k)]\cos(2k\bar{x} - 2\sigma\bar{t}) \tag{18a}$$

$$\frac{u}{\sqrt{gd}} = \pi\frac{\bar{H}}{\bar{T}}\frac{\cosh(k\bar{y})}{\sinh(k)}\cos(k\bar{x} - \sigma\bar{t}) + \frac{3}{4}\pi^2\frac{\bar{H}^2}{\bar{L}\bar{T}}\frac{\cosh(2k\bar{y})}{[\sinh(k)]^4}\cos(2k\bar{x} - 2\sigma\bar{t}) \tag{18b}$$

$$\frac{w}{\sqrt{gd}} = \pi \frac{\bar{H}}{\bar{T}} \frac{\sinh(k\bar{y})}{\cosh(k)} \sin(k\bar{x} - \sigma\bar{t}) + \frac{3}{4}\pi^2 \frac{\bar{H}^2}{\bar{L}\bar{T}} \frac{\sinh(2k\bar{y})}{[\sinh(k)]^4} \sin(2k\bar{x} - 2\sigma\bar{t}) \tag{18c}$$

where $k = 2\pi/\bar{L}$ and $\sigma = 2\pi/\bar{T}$ are the dimensionless wave number and frequency respectively, $\bar{x} = x/d$ and $\bar{y} = y/d$ are the dimensionless coordinates measured from the lower left corner, and $\bar{t} = t\sqrt{(g/d)}$ is the dimensionless time. The domain is divided by 884×132 cells in the horizontal and vertical directions, respectively. The maximum dimensionless simulation time is $\bar{t} = 136.72$, with 40,000 time steps.

In Fig. 7, the current model calculated free surface temporal variation is shown along with measurements made by Beji and Battjes [1994]. These measurements were made at the six locations shown in Fig. 6. The computational results and the experimental measurements match well. Shen and Chan [2008] simulated the same problem using a vertically uniform grid ($\Delta y = 5 \times 10^{-3} d$), with non-uniform horizontal spacing ($\Delta x_{\min} = 5 \times 10^{-2} d$). In our model, the uniform grid size is

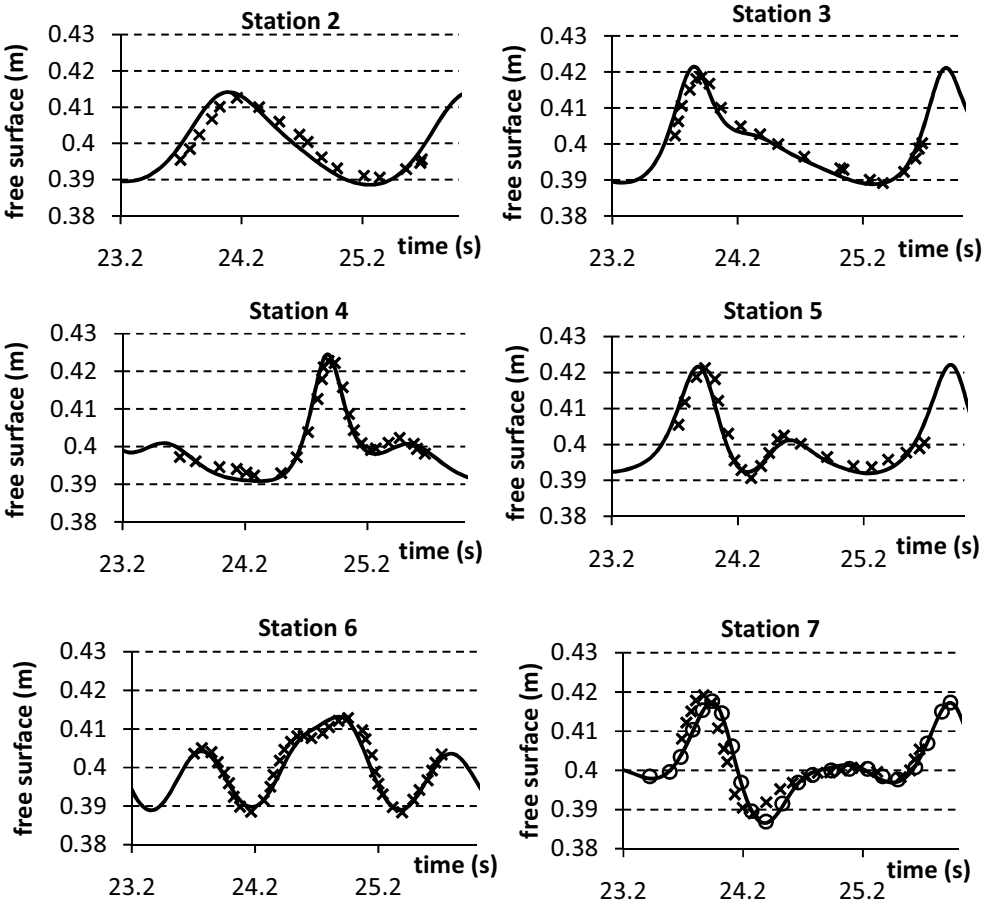

Fig. 7. Free surface versus time at the six measurement stations. The present model computations are shown as solid lines, measurements are × symbols. The results provided by Shen and Chan [2008] are shown for station 7 only with ∘ symbols.

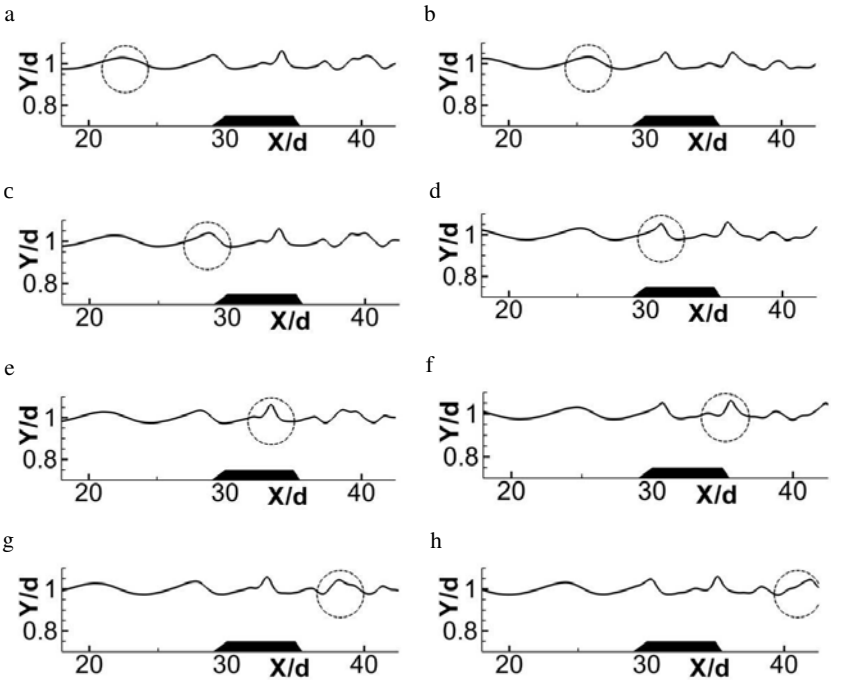

Fig. 8. Snapshots of free surface near the crest of the trapezoid at constant time interval $\Delta\bar{t} = 4.557$. A specific crest is marked with a dashed circle.

$\Delta y = 9.85 \times 10^{-3}d$ and $\Delta x = 7.7 \times 10^{-2}d$. The vertical spacing of our model is almost double the vertical spacing used by Shen and Chan [2008].

To avoid confusion, the results provided by Shen and Chan [2008] are shown for station 7 only. Their results using a relatively complicated numerical model (non-uniform grid, VOF and immersed boundary method to model obstacle presence) are almost identical to those of our simple model (uniform coarser grid, level set and blocked-off regions method).

The wave profile near the crest of the submerged bar is shown in Fig. 8. A single crest is marked by a circle for convenience. The wave profile steepens as it approaches the bar. As the wave crosses the bar, the profile is further distorted, and secondary crests appear for the initially single crested wave.

3.3. *Solitary wave propagation over a semicircular obstacle*

In this subsection, the present model capabilities are illustrated by simulating a problem of practical importance, the propagation of a solitary wave over a semicircular obstacle. The characteristics of a semicircular obstacle are expected to be similar to those of a semicircular breakwater.

Semicircular breakwaters have many engineering advantages [Sasajima *et al.*, 1994]. For instance, a zero moment is induced at the semicircle center, resulting in enhanced stability. The characteristics of this structure subject to periodic waves

were studied extensively by Yuan and Tao [2003]. On the other hand, recently the study of tsunami waves has drawn the attention of researchers [Cummins *et al.*, 2008].

Solitary waves can be utilized to investigate the characteristics of tsunami behaviors because of their hydrodynamic similarities [e.g. Hsiao *et al.*, 2008; Thao *et al.*, 2008]. Cooker *et al.* [1990] studied solitary wave propagation over semicircular obstacles extensively. They presented both experimental measurements and calculations. However, in their calculations, inviscid irrotational flow was assumed and viscosity related effects were neglected. They did not verify whether or not the flow separated behind the cylinder. Moreover, they reported failure of their numerical method when a high curvature free surface was present. An important feature of this problem is the simultaneous existence of vortices and highly deformed free surface. As already emphasized in the introduction, providing a suitable non-uniform grid (used in COBRAS, CADMAS-SURF and VOFbreak^2) for this case is relatively difficult.

The computational domain and setup are sketched in Fig. 9. Table 3 lists the dimensionless governing parameters. The values for density and viscosity ratios are identical to those given in Table 1.

We adopted two test cases: CPVD3 and CPVD2 which correspond to the experiments labeled "example 3" and "example 2" by Cooker *et al.* [1990], respectively. In these experiments, the measured wave surface heights were provided for CPVD3 at stations 1, 2 and 3, and for CPVD2 at stations 4, 5 and 6 (see Fig. 9). In Table 4, the simulation parameters for each case are listed. For both cases, the following values

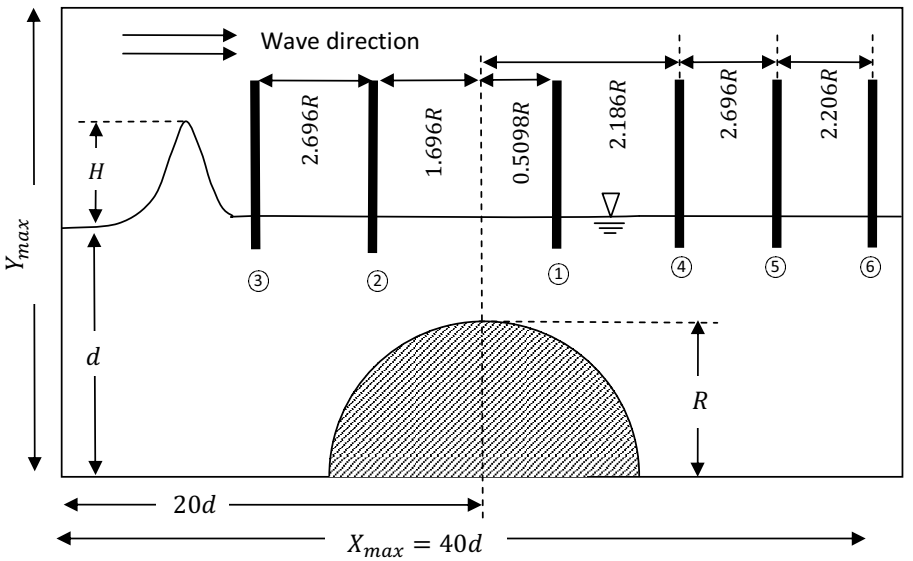

Fig. 9. Definition of the problem of solitary wave propagation over a semicircular breakwater. Refer to Table 4 for the value of $Y_{\max}$.

Table 3. Parameter definitions for solitary wave propagation over a semicircular breakwater.

Parameter	Dimensionless wave height	Reynolds number	Air-water density ratio	Air-water viscosity ratio	Dimensionless semicircular breakwater radius
Definition	H/d	$R_e = \frac{\sqrt{g}d^{1.5}\rho_w}{\mu_w}$	$\frac{\rho_a}{\rho_w}$	$\frac{\mu_a}{\mu_w}$	R/d

Table 4. Values of parameters for simulated cases.

Case	CPVD3	CPVD2
H/d	0.191	0.514
R/d	0.8	0.7
R_e	$4.03E5$	$4.92E5$
$Y_{\max}$	1.7	1.9
$t_{\max}\sqrt{g/d}$	21.908	19.093
Measurement stations	1, 2, 3	4, 5, 6

are adopted: $X_{\max} = 40$; 32,000 simulation time steps; left and right sponge layer widths of $3d$ and $0.5d$ respectively; and finally, a grid of 880×96 cells in horizontal and vertical directions respectively. Similar to Subsec. 3.1, the solitary wave peak is initiated at $X = 8d$, and the initial conditions are calculated from Eq. (15).

For validation, the free surface results using the present model are shown along with the measurements provided by Cooker *et al.* [1990] in Fig. 10. Good agreement between the computations and the experiment is evident. A slight discrepancy between the computations and the measurements is observed at station 1 in case CPVD3 and at station 2 in case CPVD2. This may be attributed to experimental errors. One source of these errors according to Cooker *et al.* [1990] was the horizontal motion of the gauges when the free surface was steep.

The presence of the separation vortex is illustrated in Fig. 11. For case CPVD2 the wave height is higher than CPVD3. As expected, more pronounced deformation of the free surface is induced for CPVD2. For CPVD3 and CPVD2, after the wave crest passes the breakwater, the free surface in the tail of the wave steepens and breaks backwards onto the cylinder. This phenomenon is pointed in Fig. 11 using a dotted circle for CPVD3 at $t\sqrt{(g/d)} = 14.605$ and for CPVD2 at $t\sqrt{(g/d)} = 14.32$.

According to the experiments performed by Cooker *et al.* [1990], the presence of this "backward breaking" phenomenon (termed as B-B) is expected. The model of Cooker *et al.* [1990] was not able to provide numerical results beyond $t\sqrt{(g/d)} \cong 14$. This is expected due to the presence of the high curvature at B-B. According to the literature review conducted, the B-B free surface feature was not emphasized before using a numerical model. The flow field in the gas region is characterized by considerably high velocities and the presence of complicated vortices. The numerical

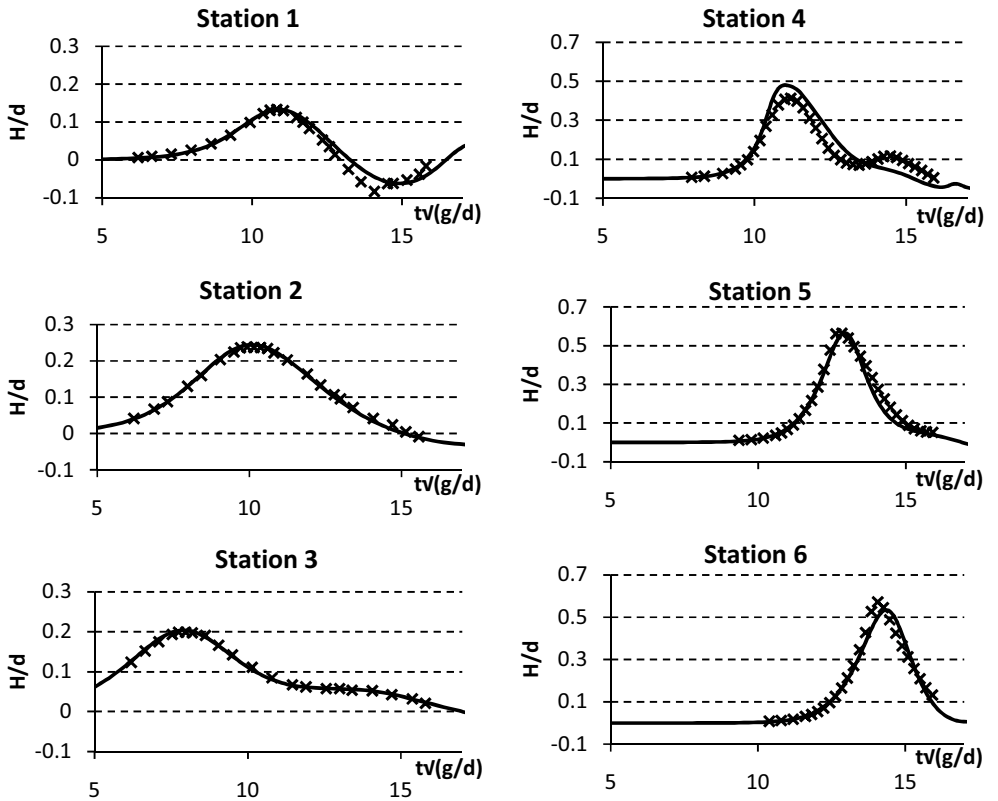

Fig. 10. Present model results (solid line) and measurements (×) of temporal free surface variation at the measurement stations reported by Cooker *et al.* [1990]. The results for CPVD3 for stations 1, 2 and 3 are to the left. The results for CPVD2 for stations 4, 5 and 6 are to the right.

results of the relatively high air velocities are already verified in Subsec. 3.1. Also the existence of air vortices near a highly deformed free surface is reasonable. The numerical results of Hieu and Tanimoto [2006] predict the occurrence of air vortices and relatively high air velocities as a wave passes a trapezoidal obstacle.

4. Conclusion and Future Work

In this paper, we have presented a new numerical multiphase model based on WENO fifth order space accurate method and the level set free surface capturing method, designed to simulate wave propagation over submerged obstacles. The model can easily handle arbitrary shaped obstacles on a uniform Cartesian grid. Consequently, the effort required to perform efficient modeling is effectively reduced. The model was validated through extensive simulations and comparisons with experimental measurements. Regarding accuracy the new model results outperformed those of other models or were at least comparable. The model was used to simulate solitary wave propagation over a rectangular obstacle. The flow velocities computed using the new model were closer to experimental data than those of COBRAS. Simulation

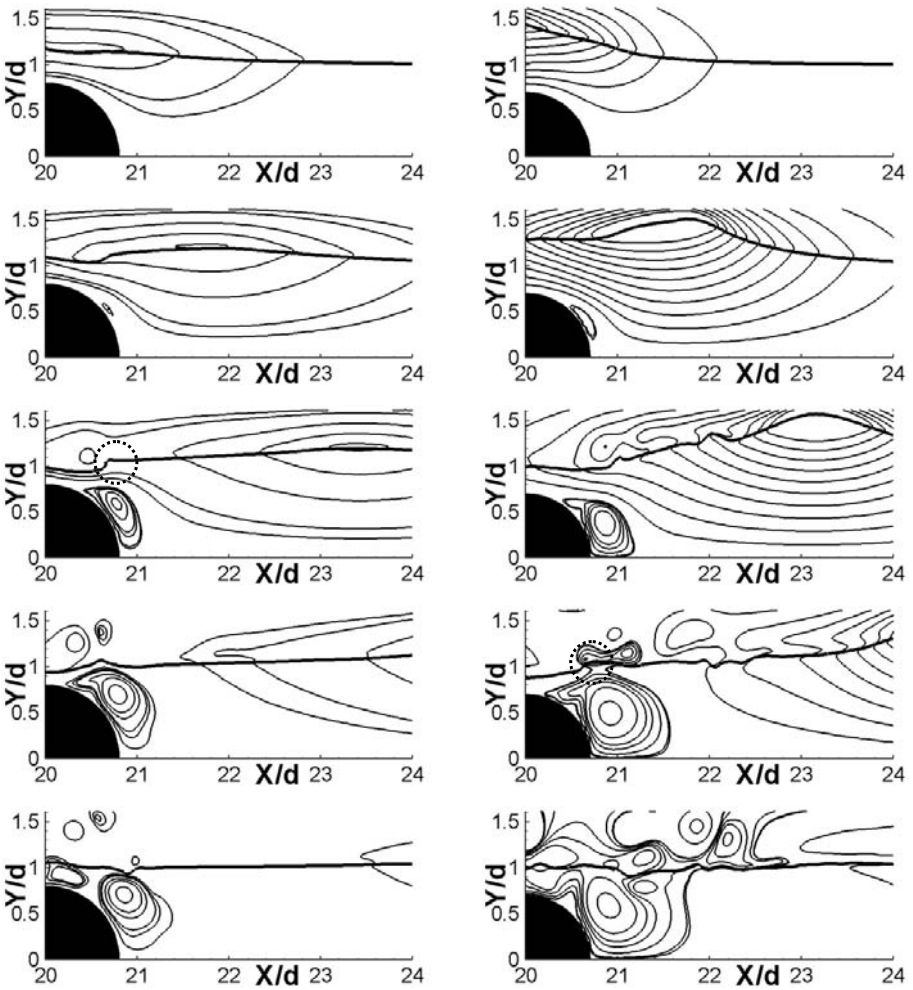

Fig. 11. Plot of stream lines and free water surface location (thick lines) during solitary wave peak passage over the breakwater. Snapshots for CPVD3 at times $t\sqrt{(g/d)} = 10.954$, 12.78, 14.605, 16.43, 18.26 are to the left. Snapshots for CPVD2 at times $t\sqrt{(g/d)} = 9.55$, 11.14, 12.73, 14.32, 15.91 are to the right.

of periodic wave propagation over a submerged trapezoidal obstacle was done. The new model free surface results agreed well with the experimental measurement and were almost identical to those produced using VOF. The model ability to capture the complicated free surface profile in the presence of a complex, vorticity-dominated flow field near the large semicircular obstacle was also revealed.

The present study concentrated only on modeling stationary obstacles using the blocked-off regions method. However, the straightforward concept of this method facilitates modeling moving obstacles. Two important applications for this problem are floating breakwaters and landslide induced waves. We are currently working on updating our model to handle these problems.

Acknowledgment

The present study is partially funded by JSPS Grant in Aid for Scientific Research (B) No. 15360263.

Appendix A. Re-Initialization

The re-initialization comprises solving Eq. (A.1), subject to the initial condition of Eq. (A.2).

$$\frac{\partial \phi_d^r}{\partial \tau} = \text{sign}(\phi_d^0)(1 - |\nabla \phi_d^u|) - \frac{\int_{\Omega_{ij}} H'(\phi_d^u)\frac{\partial \phi_d^u}{\partial t}}{\int_{\Omega_{ij}} H'(\phi_d^u) f(\phi_d^u)} H'(\phi_d^u)|\nabla \phi_d^u| \tag{A.1}$$

$$\phi_d^r(x, \tau = 0) = \phi_d^0 \tag{A.2}$$

In Eqs. (A.1) and (A.2) ϕ_d^r is the re-initialized distance function; ϕ_d^0 is the result of solving Eq. (11) by WENO and ϕ_d^u is the intermediate value computed upon solving Eq. (A.1). The functions appearing in Eq. (A.2) are defined numerically as [Sussman *et al.*, 1998]:

$$H(\phi) = \begin{cases} 1 & \text{if } \phi > \Delta \\ 0 & \text{if } \phi < -\Delta \\ \frac{1}{2}\left(1 + \frac{\phi}{\Delta} + \frac{1}{\pi}\sin\left(\frac{\pi\phi}{\Delta}\right)\right) & \text{otherwise} \end{cases}$$

$$H'(\phi) = \begin{cases} 0 & \text{if } \phi > \Delta \\ 0 & \text{if } \phi < -\Delta \\ \frac{1}{2}\left(\frac{1}{\Delta} + \frac{1}{\Delta}\cos\left(\frac{\pi\phi}{\Delta}\right)\right) & \text{otherwise} \end{cases} \tag{A.3}$$

where Δ is the grid spacing. In the present work Δ is taken as the $\max(\Delta x, \Delta y)$. A major task upon solving Eq. (A.1) is providing a stable space discretization for $|\nabla \phi_d^u|$. Such term can be discretized using a first order or second order space approximation. The first order approximation is [Osher and Fedkiw, 2002]:

$$\left(\frac{\partial \phi}{\partial x}\right)^2_{i,j} = \begin{cases} \max([\max(\phi_x^-, 0)]^2, [\min(\phi_x^+, 0)]^2) & \text{if } \phi_{i,j} > 0 \\ \max([\min(\phi_x^-, 0)]^2, [\max(\phi_x^+, 0)]^2) & \text{if } \phi_{i,j} < 0 \end{cases} \tag{A.4}$$

where ϕ_x^- and ϕ_x^+ are defined as:

$$\phi_x^- = \frac{\phi_{i,j} - \phi_{i-1,j}}{\Delta x}, \quad \phi_x^+ = \frac{\phi_{i+1,j} - \phi_{i,j}}{\Delta x} \tag{A.5}$$

The second order approximation is [Sussman *et al.*, 1998]:

$$d^1_{x,ij} = \frac{\phi_{k+1,j} - \phi_{k,j}}{\Delta x}\,, \qquad a = \frac{\phi_{k-1,j} - 2\phi_{k,j} + \phi_{k+1,j}}{(\Delta x)^2}$$

$$b = \frac{\phi_{k,j} - 2\phi_{k+1,j} + \phi_{k+2,j}}{(\Delta x)^2}\,, \qquad c = \begin{cases} a & \text{if } |a| \le |b| \\ b & \text{otherwise} \end{cases} \tag{A.6}$$

$$d^2_{x,ij} = d^1_{x,ij} - \frac{\Delta x}{2} c(2(k-i)+1)\,, \qquad \begin{matrix} d^-_x = d^2_{x,ij} & \text{if } k = i-1 \\ d^+_x = d^2_{x,ij} & \text{otherwise} \end{matrix}$$

Equation (A.6) should be repeated two times for $k = i-1$ and $k = i$. Finally, the partial derivative in x direction is calculated from:

$$\left(\frac{\partial \phi}{\partial x}\right)_{i,j} = \begin{cases} d^+_x & \text{if } (d^+_x \text{ sign}(\phi) < 0) \text{ and } (d^-_x \text{ sign}(\phi) < -d^+_x \text{ sign}(\phi)) \\ d^+_x & \text{if } (d^-_x \text{ sign}(\phi) > 0) \text{ and } (d^+_x \text{ sign}(\phi) > -d^-_x \text{ sign}(\phi)) \\ \dfrac{d^+_x + d^-_x}{2} & \text{if } (d^-_x \text{ sign}(\phi) < 0) \text{ and } (d^+_x \text{ sign}(\phi) > 0) \\ & \text{where sign}(\phi) = 2\left(H(\phi) - \dfrac{1}{2}\right) \end{cases} \tag{A.7}$$

The partial derivative in y direction can be obtained similarly. Sussman *et al.* [1998] suggested using ENO 2nd order method to obtain substantial improvement. In the present work, the 2nd order method is used at internal nodes. However at the boundary nodes, Eq. (A.4) is used due to its relatively narrow stencil. Time integration of Eq. (A.1) is done on two steps. At first, a second order Euler time integration is done

$$\phi^1_d = \phi^0_d - \Delta\tau \text{ sign}(\phi^0_d)(1 - |\nabla \phi^0_d|)\,, \quad \phi^2_d = \phi^1_d - \Delta\tau \text{ sign}(\phi^1_d)(1 - |\nabla \phi^1_d|)$$
$$\phi^3_d = \frac{\phi^1_d + \phi^2_d}{2} \tag{A.8}$$

Then, the mass conservation term is added

$$\phi^r_d = \phi^3_d - \Delta\tau \frac{\int_{\Omega_{ij}} H'(\phi^0_d) \frac{\partial \phi^r_d}{\partial t}}{\int_{\Omega_{ij}} H'(\phi^0_d) f(\phi^0_d)} H'(\phi^0_d) |\nabla \phi^0_d| \tag{A.9}$$

The integral terms in Eq. (A.9) are calculated as [Sussman *et al.*, 1998]:

$$\int_{\Omega_{ij}} g \approx \frac{\Delta_x \Delta_y}{24} \left(16 g_{i,j} + \sum_{m,n=-1;(m,n)\neq(0,0)}^{1} g_{i+m,+j+n} \right) \tag{A.10}$$

In the present work, Eq. (A.1) is advanced for 3 steps, with $\Delta\tau = (\min(\Delta x, \Delta y))/2$.

References

Barrett, R., Berry, M., Chan, T., Demmel, J., Donato, J. M., Dongarra, J., Eijkhout, V., Pozo, R., Romine, C. & Van Der Vorst, H. [1993] *Templates for the Solution of Linear Systems: Building Blocks for Iterative Methods* (Mathematical Institute, Society for Industrial Mathematics).

Beji, S. & Battjes, J. A. [1994] "Numerical simulation of nonlinear wave propagation over a bar," *Coastal Engineering* **23**, 1–16.

Chang, K. A., Hsu, T. J. & Liu, P. L. F. [2001] "Vortex generation and evolution in water waves propagating over a submerged rectangular obstacle: Part I. solitary waves," *Coastal Engineering* **44**, 13–36.

Chang, Y. C., Hou, T. Y., Merriman, B. & Osher, S. [1996] "A level set formulation of Eulerian interface capturing methods for incompressible fluid flows," *J. Comput. Phys.* **124**, 449–464.

Choi, J. I., Oberoi, R. C., Edwards, J. R. & Rosati, J. A. [2007] "An immersed boundary method for complex incompressible flows," *J. Comput. Phys.* **224**, 757–784.

Cooker, M. J., Peregrine, D. H., Vidal, C. & Dold, J. W. [1990] "The interaction between a solitary wave and a submerged semicircular cylinder," *J. Fluid Mech.* **215**, 1–22.

Cummins, P. R., Kong, L. S. L. & Satake, K. [2008] "Introduction to tsunami science four years after the 2004 indian ocean tsunami, part I: Modeling and hazard assessment," *Pure Appl. Geophys.* **165**, 1983–1989.

Dean, R. J. & Dalrymple, R. A. [1984] *Water Wave Mechanics for Engineers and Scientists* (Prentice-Hall, Inc., New Jersey).

Ekaterinaris, J. A. [2005] "High-order accurate, low numerical diffusion methods for aerodynamics," *Progress in Aerospace Sciences* **41**, 192–300.

Ferziger, J. H. & Peric, M. [2002] *Computational Methods for Fluid Dynamics* (Springer-Verlag).

Fletcher, C. A. J. [1991] *Computational Techniques for Fluid Dynamics* (Springer-Verlag).

Hieu, P. & Tanimoto, K. [2006] "Verification of a VOF-based two-phase flow model for wave breaking and wave–structure interactions," *Ocean Eng.* **33**, 1565–1588.

Hirt, C. & Nichols, B. [1981] "Volume of fluid (VOF) method for the dynamics of free boundaries," *J. Comput. Phys.* **39**, 201–225.

Hoyler, J. [1979] "Large amplitude progressive interfacial waves," *J. Fluid Mech.* **93**, 433–448.

Hsiao, S. C., Hsu, T. W., Lin, T. C. & Chang, Y. H. [2008] "On the evolution and run-up of breaking solitary waves on a mild sloping beach," *Coast. Eng.* **55**, 975–988.

Huang, C. J. & Dong, C. M. [2001] "On the interaction of a solitary wave and a submerged dike," *Coastal Engineering* **43**, 265–286.

Interim Development Committee of a Numerical Wave Flume for Maritime Structure Design [2001] *Numerical Wave Flume Theory and Development* (Coastal Development Institute of Technology — Japan) (in Japanese).

Isobe, M., Takahashi, S., Yu, S. P., Sakakiyama, T., Fujima, K., Kawasaki, K., Jiang, Q., Akiyama, M. & Oyama, H. [1999] "Interim development of a numerical wave flume for maritime structure design," in *Proc. Civil Eng. in the Ocean, JSCE*, pp. 321–326 (in Japanese).

Jiang, G. S. & Shu, C. W. [1996] "Efficient implementation of weighted ENO schemes," *J. Comput. Phys.* **126**, 202–228.

Kamphuis, J. [2000] *Introduction to Coastal Engineering and Management* (World Scientific).

Kasem, T. & Sasaki, J. [2009] "Modeling of multiphase flow using level set method and accurate hyperbolic solvers," *Ann. J. Civil Eng. in the Ocean, JSCE* 843–848.

Keulegan, G. [1953] "Characteristics of internal solitary waves," *Journal of Research of the National Bureau of Standards* **51**(3), 133–140.

Kothe, D., Juric, D., Lam, K. & Lally, B. [1998] "Numerical recipes for mold filling simulation," Report LA-UR-98-214, United States Department of Energy.

Lamb, H. [1906] *Hydrodynamics* (Cambridge University Press).
Lee, J. J., Skjelbreia, J. E. & Raichlen, F. [1982] "Measurement of velocities in solitary waves," *J. Waterway, Port, Coastal and Ocean Eng., ASCE* **108**(2), 200–218.
Lee, K. & Mizutani, N. [2009] "A numerical wave tank using direct-forcing immersed boundary method and its application to wave force on a horizontal cylinder," *Coastal Engineering J.* **51**, 27–48.
Lin, P. & Liu, P. L. F. [1998] A numerical study of breaking waves in the surf zone," *J. Fluid Mech.* **359**, 239–264.
Long, R. [1956] "Solitary waves in one and two fluid systems," *Tellus* **8**, 460–471.
Osher, S. & Fedkiw, R. [2002] *Level Set Methods and Dynamic Implicit Surfaces* (Springer).
Osher, S. & Sethian, J. [1988] "Fronts propagating with curvature dependent speed: Algorithms based on Hamilton-Jacobi formulations," *J. Comput. Phys.* **79**, 12–49.
Park, J. C., Kim, M. H. & Miyata, H. [1999] "Fully non-linear free-surface simulations by a 3D viscous numerical wave tank," *Intl. J. Numer. Meth. Fluids.* **29**, 685–703.
Patankar, S. V. [1980] *Numerical Heat Transfer and Fluid Flow* (Hemisphere).
Pilliod, J. & Puckett, E. [2004] "Second-order accurate volume of fluid algorithms for tracking material interfaces," *J. Comput. Phys.* **199**, 465–502.
Sasajima, H., Koizuka, T., Sasayama, H., Niidome, Y. & Fujimoto, T. [1994] "Field demonstration test on a semi-circular breakwater," in *Proc. Int. Conf. on Hydro-Technical Eng. for Port & Harbor Construction, HYDRO-PORT'94*, pp. 593–615.
Scardovelli, R. & Zaleski, S. [1999] "Direct numerical simulation of free-surface and interfacial flow," *Annu. Rev. Fluid Mech.* **31**, 567–603.
Sethian, J. & Smereka, P. [2003] "Level set methods for fluid interfaces," *Annu. Rev. Fluid Mech.* **35**, 341–372.
Shen, L. & Chan, E. S. [2008] "Numerical simulation of fluid-structure interaction using a combined volume of fluid and immersed boundary method," *Ocean Eng.* **35**, 939–952.
Shu, C. W. [1998] "Essentially non-oscillatory and weighted essentially non-oscillatory schemes for hyperbolic conservation laws," *Advanced Numerical Approximation of Nonlinear Hyperbolic Equations*, Lecture Notes in Mathematics, 1697, ed. Quarteroni, A., pp. 325–432.
Sussman, M. & Fatemi, E. [1999] "An efficient, interface-preserving level set redistancing algorithm and its application to interfacial incompressible fluid flow," *SIAM J. Sci. Comput.* **20**, 1165–1191.
Sussman, M., Fatemi, E., Smereka, P. & Osher, S. [1998] "An improved level set method for incompressible two-phase flows," *Computers and Fluids* **27**, 663–680.
Sussman, M., Smereka, P. & Osher, S. [1994] "A level set approach for computing solutions to incompressible two-phase flow," *J. Comput. Phys.* **114**, 146–159.
Tang, C. J. & Chang, J. H. [1998] "Flow separation during solitary wave passing over submerged obstacle," *J. Hydraulic Eng., ASCE* **124**, 742–749.
Thao, N. D., Esteban, M., Takagi, H. & Shibayama, T. [2008] "Impact pressure due to breaking solitary wave exerted on a vertical wall," in *Proc. 31st Int. Conf. Coastal Eng., ASCE*, pp. 3186–3198.
Troch, P. & De-Rouk, J. [1998] "Development of two-dimensional numerical wave flume for wave interaction with rubble mound breakwaters," in *Proc. 26th Int. Conf. Coastal Eng., ASCE*, pp. 1638–1649.
Troch, P. & De-Rouk, J. [1999] "An active wave generating-absorbing boundary condition for VOF type numerical model," *Coast. Eng.* **38**, 223–247.
Wang, Z., Zou, Q. & Reeve, D. [2009] "Simulation of spilling breaking waves using a two phase flow CFD model," *Computers and Fluids* **38**, 1995–2005.
Xiao, F. & Yabe, T. [2001] "Completely Conservative and Oscillationless Semi-Lagrangian Schemes for Advection Transportation," *J. Comput. Phys.* **170**, 498–522.
Yuan, D. & Tao, J. [2003] "Wave forces on submerged, alternately submerged, and emerged semi-circular breakwaters," *Coast. Eng.* **48**, 75–93.

Zhang, J. & Jackson, T. L. [2009] "A high-order incompressible flow solver with WENO," *J. Comput. Phys.* **228**, 2426–2442.

Zhuang, F. & Lee, J. J. [1996] "A viscous rotational model for wave overtopping over marine structure," in *Proc. 25th Int. Conf. Coastal Eng., ASCE*, pp. 2178–2191.